Research Article | Vol. 30, No. 24 / 21 Nov 2022 / Optics Express 43104
Optics EXPRESS

Enhanced light–matter interactions in ultrathin transition-metal-dichalcogenide metasurfaces by magnetic and toroidal dipole bound states in the continuum

XUEYANG ZONG,[1] LIXIA LI,[1,2] KUN YU,[1] AND YUFANG LIU[1,*]

[1] *Henan Key Laboratory of Infrared Materials & Spectrum Measures and Applications, School of Physics, Henan Normal University, Xinxiang 453007, China*
[2] *lixia_li@htu.edu.cn*
[*] *liuyufang2005@126.com*

Abstract: Nonradiating states of light have recently received a lot of attention in nanophotonics owing to their ability to confine and enhance the electromagnetic fields at the nanoscale. Such optical states not only offer a promising way to overcome the problem of losses associated with plasmonic materials, but also constitute an efficient platform for interaction of light and matter. Here, we report the radiationless states in compact, ultrathin transition-metal-dichalcogenide metasurfaces, namely bound states in the continuum (BICs). Through applying the multipole analysis to the BIC-based metasurfaces, we demonstrate that the BICs can be classified as magnetic dipole (MD) and electric toroidal dipole (TD) modes, both of which correspond to the Γ-point symmetry-protected BIC. Due to the large field confinement inside the nanoresonators originating from the BICs, the strong coupling is realized between quasi-BICs and the exciton resonance, showing that the Rabi splitting energy can be up to 134 meV and 162 meV for the MD and TD quasi-BIC, respectively. We reveal that reduction of the effective mode volume is highly responsible for the enhancement of coupling strength. Furthermore, it is demonstrated that a large mode volume can lead to increase of the field leakage, which enables our metasurfaces to find applications in, for instance, label-free sensing based on refractometric detection.

1. Introduction

Bound states in the continuum (BICs) in optics are a localized state that coexists with a radiation continuum but completely decouples from the continuum. Therefore, an ideal BIC has a radiative lifetime that diverges to infinity and cannot be inaccessible from external excitations that belong to a same continuum. Nevertheless, in practice, owing to finite size samples, material absorption, and other external perturbations, the state can couple with the external radiation and collapse to a leaky resonance with a finite lifetime—a regime referred to as quasi-BIC [1,2]. Now, quasi-BICs have been utilized to gain very high-Q resonances that possess strong electromagnetic-field enhancement. Such resonances are demonstrated to hold vast potential for a myriad of applications in both linear and nonlinear optics, including lasing [3], sensing [4,5], filters [6], enhanced harmonic generation [7,8], and many others. Thus, it is of paramount importance to access quasi-BICs and harness their functionalities in practical applications. Recently, resonant nanostructures have opened a new paradigm for realization of quasi-BICs in nanophotonics, such as dielectric photonic crystals [9], optical waveguides [10], hybrid photonic-plasmonic systems [11], all-dielectric resonant meta-atoms and metasurfaces [12–15]. Among them, high-refractive-index dielectric metasurfaces with subwavelength confinement properties have been a fascinating platform, which allow us to create BIC states by engineering the structural symmetry of the elementary scattering units supporting Mie resonances.

#474088 https://doi.org/10.1364/OE.474088
Journal © 2022 Received 25 Aug 2022; revised 19 Oct 2022; accepted 27 Oct 2022; published 8 Nov 2022

Optics EXPRESS

Of late, transition metal dichalcogenides (TMDCs) have sparked a great deal of attention and interest of research in terms of creating novel dielectric metamaterials with high refractive index. TMDCs are van der Waals materials, and in particular, they exhibit a direct bandgap in the atomic monolayer limit, making them interesting for various optoelectronic applications, such as ultrafast modulation [16], light emission [17], photodetection and light harvesting [18], as well as for fundamental investigations of strong light–matter interactions [19–21]. Bulk TMDC materials possess naturally very high in-plane refractive indices in the visible and near-infrared spectral range, higher than what is found in widely used dielectric materials with high refractive index, as silicon and III–V semiconductors. Compared to these traditional dielectric materials like silicon, TMDCs are capable of simultaneously boosting the second- and third-harmonic generation in the context of nonlinear light emission [22]. Besides, since layered TMDCs have strong van der Waals stiction forces, they can be patterned on low-refractive-index transparent substrates. This is not readily realized for III–V materials. To date, bulk TMDCs have been utilized for designing nanostructures including photonic crystals [23,24], metasurfaces [22,25], and other structures depending on the strong photon–exciton coupling [26]. Nevertheless, it has remained elusive how to excite and control radiationless BIC states in TMDC-based metasurfaces.

In this work, we demonstrate the generation of BICs in TMDC metasurfaces consisting of narrow-gap WS_2 nanobar arrays. The high refractive index in excess of 4 for the bulk WS_2 allows for optical resonances in nanoresonators with small dimensions, enabling densely packed metasurfaces. The WS_2 metasurfaces are demonstrated to support multiple symmetry-protected BICs at the Γ point which can be represented by magnetic dipole (MD) and electric toroidal dipole (TD) modes. Through introduction of defects and perturbations that break the structural in-plane symmetry, such MD- and TD-BIC modes can be transformed into high-Q quasi-BICs with dominating magnetic and toroidal dipole excitations respectively, at the normal incidence of light. Because the quasi-BIC is always accompanied by a giant electromagnetic-field enhancement in the interior of structure, we show that our metasurfaces by themselves provide a natural platform for light–exciton interaction. Specifically, it is observed that MD and TD quasi-BICs strongly coupled to the WS_2 exciton lead to Rabi splittings of up to 134 meV and 162 meV, respectively. We reveal that the difference between Rabi energies for MD and TD BICs can be attributed to their different mode volumes. We demonstrate that a small mode volume allows us for observation of the large spectral splitting, while a large one is more favorable to improving the sensing performance of BIC modes.

2. Results and discussion

The design of our TMDC-based WS_2 metasurface is illustrated in Fig. 1(a). It consists of a periodic square array of two identical nanobars, placed on a low-refractive-index substrate (SiO_2). We indicate as P the period of structure, H the thickness of WS_2 nanoresonator and G the gap width between nanobars. In all cases, both the lengths of two nanobars and the sum of their widths and gap satisfy $L = 0.8P$, as shown the top-left-corner inset in Fig. 1(a). We first consider the passive case of the metasurface (that is, the Lorentz oscillator is taken out in the dielectric function of WS_2, as illustrated in Appendix 1) and calculate its band structure along the MΓ and ΓX directions using the three-dimensional finite-element-method eigenfrequency solver by Comsol Multiphysics. Here, Γ, X, and M represent the high-symmetry points of the first Brillouin zone for a square lattice. This is shown in Fig. 1(b), where the structural parameters are $P = 300$ nm, $H = 30$ nm, $L = 240$ nm, and $G = 0.1P = 30$ nm. We observe that there are four modes with different dispersion in the band structure near the Γ point, wherein modes 1, 2 and 3 correspond to the transverse electric (TE)-like mode and mode 4 to the transverse magnetic (TM)-like mode. Figure 1(c) shows the Q factors of these four modes as a function of Bloch wavevector. It is found that the Q factors are appreciably high for modes 1 and 3 and drop sharply away from the Γ point, manifesting that the two modes correspond to symmetry-protected BICs at the Γ point.

Optics EXPRESS

For modes 2 and 4, they have a large leakage and remain Q factor lower than 10^3 over the entire wavevector span of interest, which allows for the probing via far-field measurements.

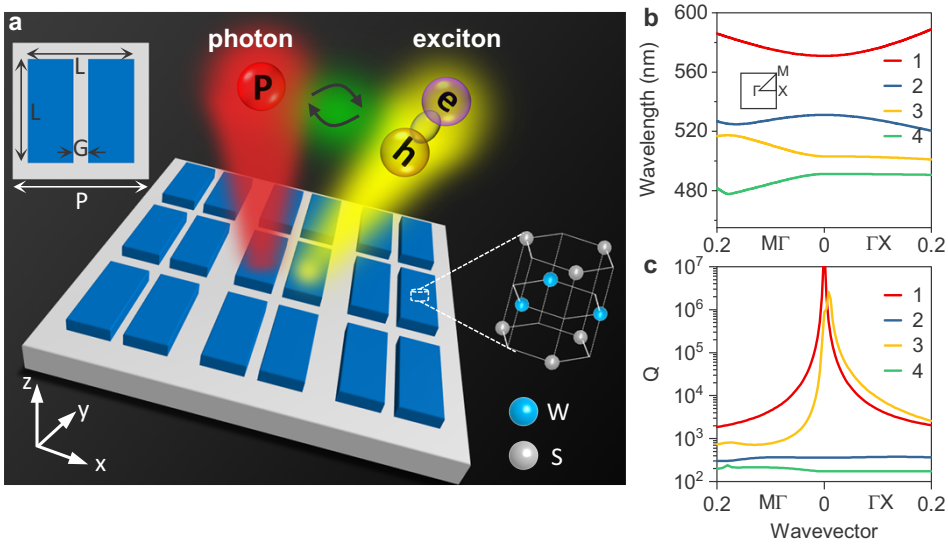

Fig. 1. BIC-based TMDC metasurfaces. (a) Schematic of the WS_2 metasurface on a silica substrate. The structure is composed of a square lattice with unit cells consisting of two identical WS_2 nanobars, the dimensions of which are the period P, the gap between nanobars G, the length of a nanobar L and its width $W = (L - G)/2$, as shown in the top-left-corner inset. The bottom-right-corner inset sketches the lattice structure of the 2H-stacked WS_2. (b) Dispersion relation and (c) Q factors of four eigenmodes in both the MΓ and ΓX directions as a function of Bloch wavevector. The inset in (a) represents the first Brillouin zone of the square lattice. The calculations are performed at structural parameters: $P = 300$ nm, $L = 0.8P$, $G = 0.1P$, and WS_2 thickness $H = 30$ nm.

2.1. *Multipolar origination of the BICs*

Next, we apply the multipole analysis to our metasurface to get a comprehensive understanding of these modes, as shown in Fig. 2(a–c). Through using the Cartesian multipole decomposition, we calculate the TD (Fig. 2(a)), electric dipole (ED) (Fig. 2(b)) and MD (Fig. 2(c)) moments for the four eigenmodes at the Γ point. It can be seen from Fig. 2(a) that modes 2 and 4 assume a predominant TD character, of which the TD moment is along the y and x axis (that is, TD moment T_y and TD moment T_x), respectively. Such TD modes are different to the nontrivial ones that have a TD moment along z axis while they are dependent on the lattice constant. Since our metasurface is at the sub-diffractive regime and has the C_2 symmetry, the TD moment cannot contribute to the far-field radiation along z-axis direction. However, the ED mode plays a crucial role in opening the radiation channel able to couples to the outgoing waves, as shown in Fig. 2(b). Among the four modes, only modes 2 and 4 have a large ED moment and are with the ED mode P_y and the ED mode P_x, respectively. This manifests that modes 2 and 4 can be respectively excited by the normally incident plane wave with polarization parallel to the y and x direction. For modes 1 and 3, they are radiationless due to their very small ED moments that cannot couple to the radiating waves, and nevertheless, both of them exhibit dominating MD moments along the z direction (see Fig. 2(c)). Such the out-of-plane MD is "dark" and cannot be directly excited by normal incident light. Thus, modes 1 and 3 can also be referred to as the MD BIC.

Optics EXPRESS

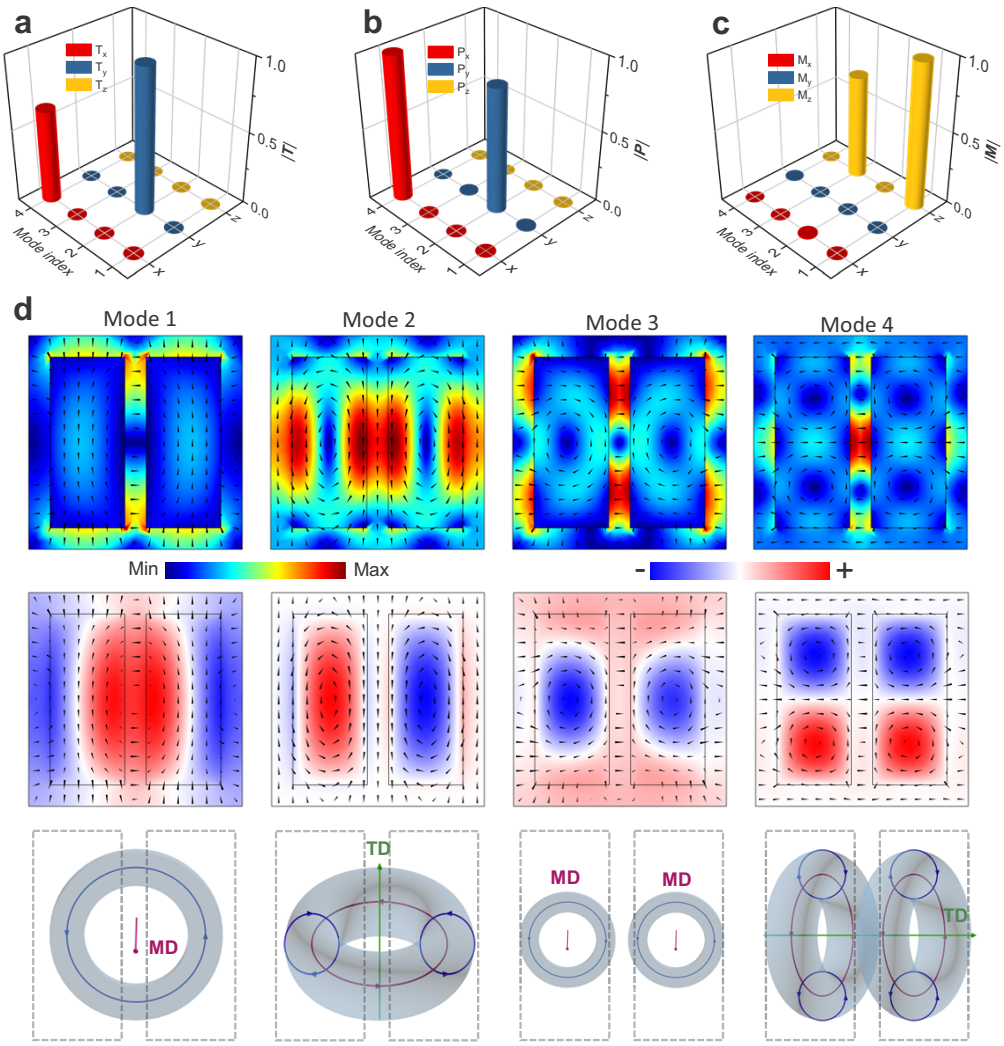

Fig. 2. Multipole analysis to the BIC-based WS_2 metasurface. (a–c) Multipole decomposition results of the eigenmodes at the Γ point, which are normalized to their maximum within each panel. **T**, **P**, and **M** respectively are the toroidal, electric, and magnetic dipole moments. (d) Top row, the *xy* cross-sectional electric-field profiles $|E|$ for the Γ-point modes, calculated by through the center of the unit cell, $z = 0$; middle row, corresponding z component of the magnetic field, H_z; lower row, sketches of the magnetic **M** and the toroidal **T** dipole moments. The black arrow in the field distributions stands for the electric-field vector.

In order to gain a deeper insight into the configuration of these modes, we plot in Fig. 2(d) the electric-field distributions for these four modes. It is obvious that the excitation of the MD mode is accompanied by a circulating electric field (see the mode 1), while the mode 3 exhibits two circulating electric fields with in-phase oscillation in each nanobar, thus leading to two parallel MD moments along the z direction. The TD moment is associated with both the circulating magnetic field and the electric poloidal current distribution. This can be seen from the field profiles of modes 2 and 4. For the direction of their TD moments, it can be visualized from the vivid schematics in the bottom row of Fig. 2(d), which validates the multipole decomposition results in Fig. 2(a).

Optics EXPRESS

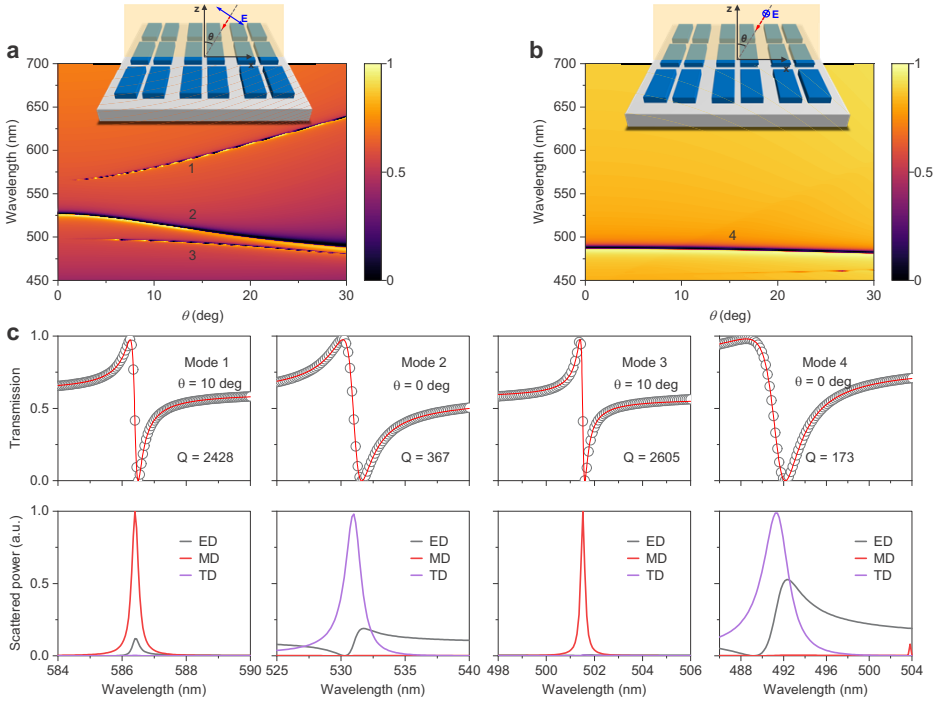

Fig. 3. Far-field spectral features for the WS_2 metasurface. (a, b) Angle-resolved transmission spectra along the ΓX direction for the WS_2 nanostructure illuminated by (a) TE- and (b) TM-polarized plane waves. (c) Top row, detailed transmission of the four modes, with open circles being the transmittance calculated from finite element method and solid lines the fitting results from eq 1; bottom row, normalized radiated power of the modes to which the Cartesian multipoles contribution, corresponding with the panels in top row.

For the sake of getting a better sense of how light propagates in the metasurface, we calculate the far-field spectra of the structure illuminated by an incident light with different polarizations. In this work, the polarization of light along the y direction is defined as TE and along the x direction as TM. As seen Figs. 3(a) and 3(b), they display the calculated TE- (Fig. 3(a)) and TM-polarized (Fig. 3(b)) transmission spectra with respect to incident angle θ along the ΓX direction. The TE band diagram shows three resonances which are corresponding to eigenmodes 1, 2 and 3 in Fig. 1(b). According to the above-mentioned eigenfrequency analysis, MD modes 1 and 3 are the symmetry-protected BIC at the Γ point and thus exhibit vanishing linewidths at the normal incidence. With increase of the incident angle, they have growing losses and are transformed into the leakage resonances called as quasi-BICs. Under TM-polarized light (Fig. 3(b)), only one resonance appears in the transmission map, corresponding to the TD mode 4. Both TD modes 2 and 4 show a relatively broad resonance at a wide angular range due to their low Q factors. These results are well in accordance with those of the eigenmode analysis.

To further observe their spectral features, we give the transmission for these four resonance modes, as shown in the top-row panels of Fig. 3(c) (open circles), where MD resonances (modes 1 and 3) and TD resonances (modes 2 and 4) are plotted at $\theta = 10$ deg and 0 deg, respectively. Both two resonances manifest themselves as a pronounced asymmetric Fano line shape in the far-field spectral response. As we all know, Fano or Fano-like resonance is formed originating from the interaction between a "bright" state and a "dark" state. For optical resonances studied here, the MD and TD are "dark" while the ED is "bright" and forms a leaky channel that couples

Optics EXPRESS

to the free-space radiation. This coupling determines the spectral bandwidth. To this end, we first derive the Q factor of each mode from the corresponding transmission spectrum by fitting the transmission T as a function of frequency, to a Fano line shape given by

$$T(\omega) = A + B\frac{(q\gamma+\omega-\omega_0)^2}{\gamma^2+(\omega-\omega_0)^2} \tag{1}$$

where γ describes the overall damping rate of the resonance, ω_0 is the resonant frequency defining the position of the Fano-like feature, q is the parameter characterizing the asymmetry of the resonance profile, and A and B are constant that respectively describe the background and the overall peak height. The fitting results are shown by the solid lines, which nearly perfectly reproduce the transmittance. According to the formula $Q = \omega_0/2\gamma$, the Q factor can be estimated as 2428, 367, 2605 and 173 for modes 1 to 4, respectively. Then, we execute the multipolar expansion for the modes. As shown in the bottom-row panels of Fig. 3(c), the normalized radiated power of the four modes is calculated, contributed by the ED, MD and TD. It is evident that the excitation of ED becomes smaller as the Q factor increases. Specially, the Fano resonances can collapse to a pure bound state with infinite Q factor within the light cone when access to radiation channel is prohibited due to the extremely small ED. For symmetry-protected MD BICs, the light normally incident to the metasurface can be used for triggering the transition from quasi-BICs to BICs. We next show the TD mode 2 can also become an ideal BIC via choosing proper structural dimensions of the nanobars.

2.2. Manipulating the BICs under normal excitations

Figure 4(a) shows the transmission of the metasurface excited by a normally y-polarized plane wave, as a function of the gap width between two symmetric nanobars, where other geometrical parameters remain unchanged and the parameter associated with the gap width is $\eta = G/P$ (see the inset in Fig. 4(a)). It can be seen that at a value of $\eta = 0.2$, the spectral linewidth of the TD resonance entirely vanishes. This is attributed to the fact that the structure can be viewed as an equidistant grating when $\eta = 0.2$, and in this situation, the resonance cannot be excited due to the momentum mismatch between the incident photon and the waveguide mode. Further, we calculate in Fig. 4(b) the Q factor of the eigenmodes as a function of η, showing that there is an eigenmode with a diverging Q factor at $\eta = 0.2$, which manifests the formation of a BIC. The electromagnetic-field distribution in the inset of Fig. 4(b) further reveals the nature of TD for the BIC. It should be noted that the BIC is also symmetry-protected at the Γ point.

Additionally, we demonstrate that introducing the symmetric defects to the structure can provide an efficient way opening the leaky channel so that the MD quasi-BIC can be excited under normal incidence. As shown in the inset of Fig. 4(c), the Δ is defined as a parameter determining the amount of the structural symmetry-breaking, which is the offset of the air gap away from the center of the unit cell along the x direction (short side of nanobars). Here, we fix the gap width at $G = 0.2P$ to avoid the excitation of TD resonances, and calculate the transmission map as a function of Δ for the asymmetric metasurfaces under y polarized light at incident angle of $\theta = 0$ deg. As shown in Fig. 4(c), the transmission dip vanishes at the zero offset due to the lack of the coupling between the incident light and the BIC. A narrow dip occurs in the transmission spectra as the structural symmetry is broken, and it becomes broader with increase of the offset value. This corresponds to the formation of the MD quasi-BIC and a decrease of the Q factor (Fig. 4(c)), respectively.

2.3. Strong coupling between BICs and exciton

The generation of BICs is accompanied by the giant electromagnetic-field enhancement inside structures, indicating that they can be used for boosting light–matter interactions. To this end, strong coupling between BICs and the exciton is explored in our metasurface. To observe

Optics EXPRESS

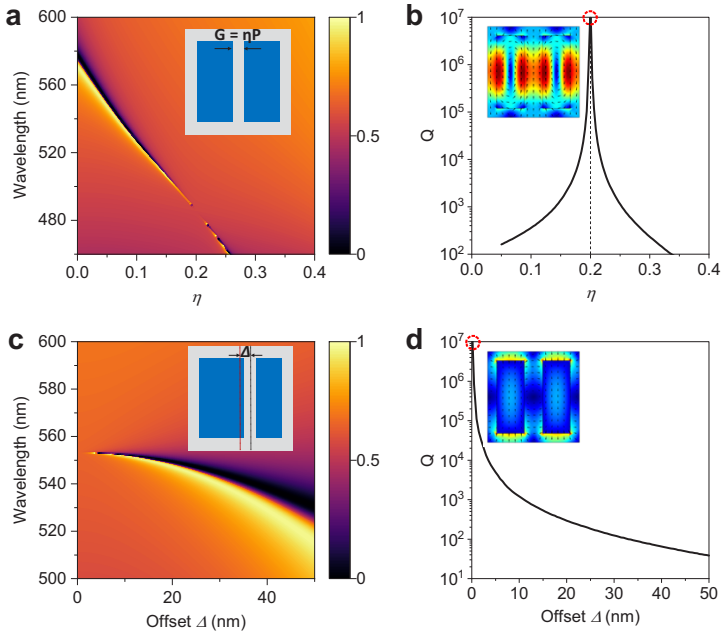

Fig. 4. Control over the BICs in WS_2 metasurfaces at normal incidence. (a, b) Transmission spectra and Q factors with respect to the parameter η for the symmetric metasurface. (c, d) Transmission spectra and Q factors with respect to the offset Δ of a gap for the asymmetric metasurface, calculated when the width of gap is fixed at $G = \eta P = 0.2P$. Insets in (b, d) show the electric-field profiles for the ideal BICs highlighted by red-dotted circles. All calculations are carried out in the case where the nanostructures are normally illuminated by a plane wave polarized parallel to the long side of nanobars (y axis).

this coupling, we consider the active structure for which the WS_2 exciton is turned back on. Figures 5(a–c) show the optical response for three structural configurations that respectively support the TD quasi-BIC (Fig. 5(a)), the TD resonance (Fig. 5(b)), and the MD quasi-BIC (Fig. 5(c)), where the absorption at normal incidence is plotted as a function of the period P. For the TD-BIC metasurface where the gap width between two nanobars is fixed at $G = 0.1P$, the absorption map exhibits clear anticrossing between the TD quasi-BIC and exciton modes, splitting into upper and lower energy branches with dispersive character. This marks the strong coupling and the formation of the mixed optical state consisting of BIC and exciton. In particular, the mix state in the lower (upper) energy branch takes on a more BIC (exciton) character for sparse arrays (large period). Moreover, the anticrossing appears at the spectral position at which the uncoupled BIC and exciton modes are tuned to intersect, which results in a spectral splitting of 162 meV (see Figs. 5(a) and 5(d)). In order to confirm this, the strong coupling between a BIC and exciton mode is modeled using the following coupled oscillator model

$$E_{\pm} = \tfrac{1}{2}[E_{BIC} + E_{ex} + i(\gamma_{BIC} + \gamma_{ex})] \pm \sqrt{g^2 + \tfrac{1}{4}[E_{BIC} - E_{exc} + i(\gamma_{ex} - \gamma_{BIC})]^2}, \tag{2}$$

where $E_{\pm}$ is the energy of the coupled upper and lower branches related to the lattice period, E_{BIC} and E_{ex} are the energy of the uncoupled BIC and exciton modes, respectively, γ_{BIC} and γ_{ex} are the half width at half maximum of the uncoupled BIC and exciton modes, respectively, and g is the coupling strength between BIC and exciton. At zero detuning, that is, $E_{BIC} - E_{ex} = 0$, the Rabi splitting energy amounts to $\Omega = 2\sqrt{g^2 - \frac{1}{4}(\gamma_{exc} - \gamma_{BIC})^2}$. In this model, the uncoupled BIC energy can be obtained from the period-dependence transmission of the passive structure, while

Optics EXPRESS

the uncoupled exciton energy is set to $E_{ex} = 2$ eV corresponding to the absorption frequency of the bulk WS_2 membrane. The dispersion relation of the hybrid BIC–exciton state obtained from the coupled oscillator model is shown in Fig. 5(d), which quantitatively matches that from the absorption spectra.

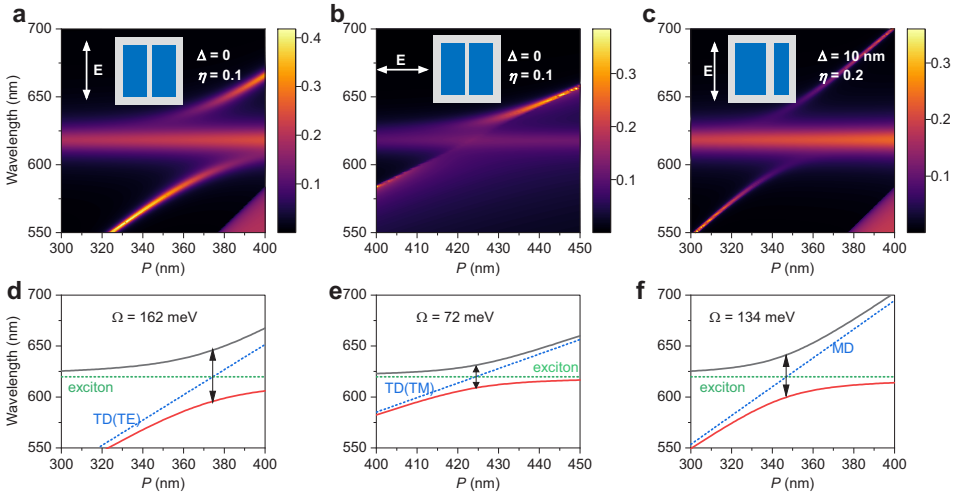

Fig. 5. Strong coupling of nonradiating states with excitons in WS_2 metasurfaces. (a–c) Absorption spectral maps as a function of the lattice period for three WS_2 metasurfaces. Insets show schematic of the structure designs and the polarization configurations. (d–f) Theoretical dispersion curves of coupled upper/lower polariton branches (solid red/black curves) resulting from strong coupling between bare optical resonance/exciton dispersion curves (dotted blue/green lines), corresponding with panels (a–c), respectively.

In addition to observation of the clear anticrossing, that strong coupling is confirmed requires to satisfy the following inequality:

$$\Omega > \gamma_{BIC} + \gamma_{ex} \tag{3}$$

This implies that coherent energy exchange between the two modes occurs in the strong coupling regime at a rate faster than the decay rate of each mode. Our system (Fig. 5(a)) rigorously meets this criterion, with $\Omega = 162$ meV, $\gamma_{BIC} = 3$ meV, and $\gamma_{ex} = 28$ meV. When the polarization of incident light is switched to being along the x-axis direction (that is, TM polarization), the resulting Rabi splitting as small as 75 meV is observed, as shown in Figs. 5(b) and 5(e). This is because the electromagnetic field is mainly confined inside gap in this case, which cannot interact with the exciton. Same studies are performed for the MD-BIC metasurface, as seen in Fig. 5(c). In the asymmetric structure with the offset of $\Delta = 10$ nm and the gap width of $G = 0.1P$, the strong coupling between the MD quasi-BIC and exciton modes produces a 134 meV spectral splitting (Figs. 5(c) and 5(f)).

The coupling between photon and exciton scales as $\Omega \propto \sqrt{nf/V_{eff}}$, where n, f, and V_{eff} represent oscillator numbers per volume, exciton oscillator strength, and effective mode volume, respectively. For bulk WS_2, the effective concentration of excitons has been determined at the fabrication stage (that is, n and f are a definite value), and thus, the mode volume is an appropriate figure of merit that can provide a quantitative insight into the difference of the Rabi splitting of these coupled systems. The definition of mode volume V_{eff} can be given using the equation

$$V_{eff} = \frac{\int_V |\boldsymbol{E}(r)|^2 d^3r}{\left(\int_{V_0} |\boldsymbol{E}(r)|^2 d^3r\right)/V_0} \tag{4}$$

Optics EXPRESS

where V is the simulation volume, V_0 is the actual volume of nanobars, and $\boldsymbol{E}$ is the electric field. According to eq 4, we calculate the effective eigenmode volume for the three architectures, which is potted as a function of the lattice period. As shown in Fig. 6, the effective mode volumes V_{eff} of the three modes display an increasing trend due to the increase of optical cavity dimension as the period increases. And the TD resonance for the TE-polarized incidence has a smallest mode volume among them, thus resulting in a largest Rabi splitting energy between TD quasi-BIC and exciton. For the other two modes, the difference of corresponding Rabi splitting is also explained well by their effective mode volumes. Reduction of the effective mode volume is therefore responsible for the observed increase in the Rabi splitting. Furthermore, one can note that the effective mode volume V_{eff} is always larger than the physical volume V_0 (shown by the dashed line), which manifests that there is a portion of field leakage into the surroundings. This makes our metasurfaces a potential sensing platform.

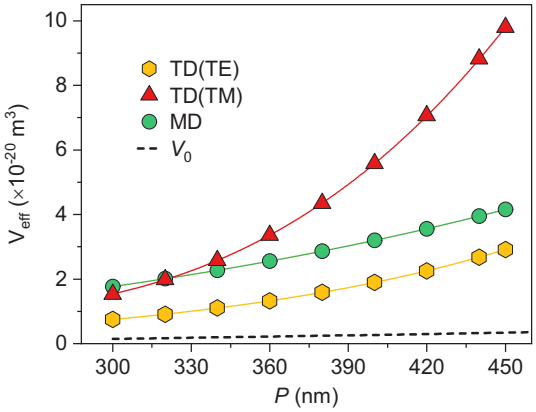

Fig. 6. Effective modal volume of the three optical states in WS_2 metasurfaces as a function of period. The solid lines are to guide the eyes. The dashed line indicates the actual volume of nanobars.

To this end, we study how the far-field spectrum for BIC-based metasurfaces is modified upon changing the refractive index of the incident medium. Figure 7(a) shows the variations within the absorption spectral response of the TD-BIC metasurface, demonstrating that as the refractive index increases, the TD quasi-BICs (indicated by an orange shadow) shift to longer wavelengths. This change can also be observed in the MD-BIC metasurface (Fig. 7(d)), whereas the MD quasi-BIC clearly shows larger spectral shifts than the TD quasi-BIC as due to its larger mode volume. A larger mode volume implies the electromagnetic field is confined within the dielectric layer with higher evanescent leakage, thus leading to a higher sensitivity. This leakage can be further increased by reducing the thickness of the metasurface, which can be used for boosting the sensitivity of photonic sensors. As shown in Figs. 7(b) and 7(e), we plot the linear dependence of the resonance wavelength of TD quasi-BIC (Fig. 7(b)) and MD quasi-BIC (Fig. 7(e)) to the refractive index of the incident medium at different thicknesses of metasurfaces, and calculate corresponding refractive index sensitivity (S) that is defined as the ratio of the resonance wavelength to the change in the refractive index of the adjacent medium (that is, $S = \Delta\lambda/\Delta n$). These results clearly show that reducing the thickness can effectively improve the sensitivity. Also, we show the influence of the gap width G (Fig. 7(c)) and the offset Δ (Fig. 7(f)) on the sensitivity. As can be seen, the sensitivity is robust against these two parameters, which in turn indicates that the effective mode volume dose not vary much (see Appendix 4). However, since the resonance Q factor strongly depends on these two parameters (see Figs. 4(b) and 4(d)), we can by properly choosing parameters obtain an extremely high sensing figure of merit (not

Optics EXPRESS

shown), a crucial performance-defining parameter obtained by dividing the sensitivity by the full width at half maximum of the resonance. Finally, we would like to remark that there is still a plenty of room for improving the results reported here by, for example, reducing the thickness of WS_2 to the monolayer level or by removing the substrate. This is because at the atomically thick WS_2 membrane, the field leakage will be substantially increased. And suspending the structure in space can effectively increase the interaction volume between light and analyte. In order to illustrate this idea, we take the TD-BIC metasurface as an example, and show in the Appendix 5 its refractive index sensitivity when suspended in the environment. It is evident that the freestanding structure exhibits a higher sensitivity than the one placed on a substrate. More remarkably, a sensitivity of up to 480 nm/RIU can be achieved in the structure with a few-layer WS_2 thickness, which can be comparable to that of plasmonic nanostructures.

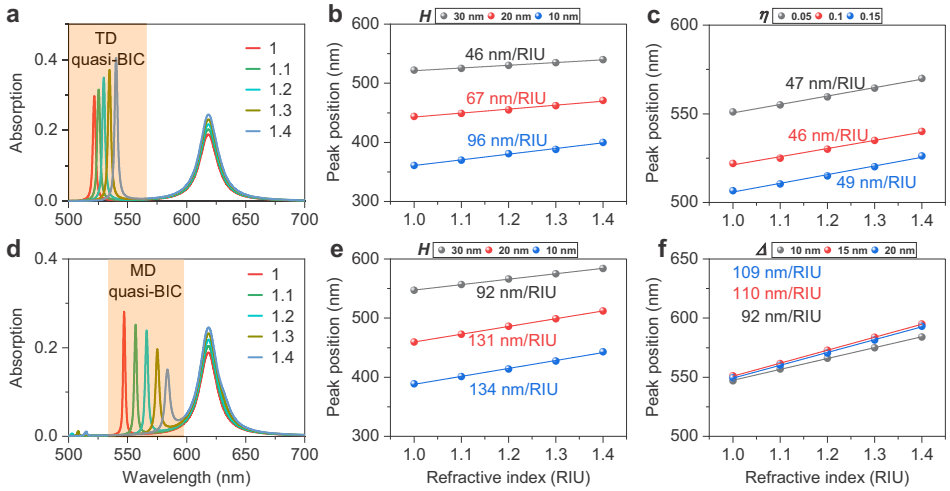

Fig. 7. BIC-based metasurfaces for refractive-index sensing. (a, d) Normal-incidence absorption spectra of (a) the TD-BIC metasurface (initial parameters: $P = 300$ nm, $L = 0.8P$, $\eta = 0.1$, $\Delta = 0$ nm, and $H = 30$ nm) and (d) the MD-BIC metasurface (initial parameters: $P = 300$ nm, $L = 0.8P$, $\eta = 0.2$, $\Delta = 10$ nm, and $H = 30$ nm) for different values of the refractive index of the incident medium. (b, c) Linear plot of TD quasi-BIC shifts as a function of refractive index for (b) different values of H and (c) for different values of η. (e, f) Linear plot of MD quasi-BIC shifts as a function of refractive index for (b) different values of H and (c) for different values of Δ. Note that when changing the structural parameters of interest (H, η, and Δ), other initial parameters are fixed.

3. Conclusion

In summary, we have demonstrated that the ultrathin resonant WS_2 metasurface supports MD BICs with out-of-plane MD moments and TD BICs with in-plane TD moments. Through either tuning of the system parameters or manipulating the symmetry of the excitation field, we can transform the BICs into the high-Q leaky resonances. Using the multipole decomposition approach, we have shown that the ED moment plays an important role in opening a radiation channel and transforming the BICs into the leaky resonances. Since the BICs can produce strong light confinement within the nanoresonators, the strong coupling regime was observed in our metasurface where the WS_2 serves as a host for both excitonic and cavity modes, without the need of an external optical cavity. Finally, we demonstrated the promise of the WS_2 metasurface for sensing applications. Our studies could pave the way for making integrated polaritonic devices, as well as for TMDC-based light harvesting.

Optics EXPRESS

Appendix 1: Numerical simulations

The simulations of transmission and absorption maps of structures have been done using the rigorous coupled wave analysis [27]. The band structures, Q-factor, multipole analysis, and electromagnetic-field simulations have been carried out using a commercial software based on finite element code (COMSOL Multiphysics). All results were obtained by simulating a unit cell with Floquet periodic boundary conditions in the two lattice-vector directions and perfectly matched layers at the boundaries in the out-of-plane direction.

Appendix 2: Bulk WS_2 model

The dielectric function of bulk WS_2, used in numerical simulations and analytical calculations, is given by [28]

$$\epsilon(E) = \epsilon_0 + \frac{f_0}{E_{ex}^2 - E^2 - i\gamma_{ex}E}, \tag{5}$$

where $\epsilon_0 = 20$ is the permittivity of the passive structure, $f_0 = 0.8$ eV^2 is the oscillator strength of WS_2 exciton, and $E_{ex} = 2$ eV and $\gamma_{ex} = 50$ meV are its energy and linewidth, respectively. For the WS_2 metasurface, when taking the Lorentz term out, it is called the passive structure, otherwise it is called the active structure.

Appendix 3: Cartesian multipole decomposition

Cartesian multipoles are computed by integrating over the charge density $\rho(\mathbf{r})$ or current density $\mathbf{J}(\mathbf{r})$ distribution within the unit cell of the metasurface. And the dipole moments can be calculated by [29]:

$$P_\alpha = \frac{1}{i\omega} \int d^3r \, J_\alpha, \tag{6}$$

$$M_\alpha = \frac{1}{2c} \int d^3r \, [\mathbf{r} \times \mathbf{J}]_\alpha, \tag{7}$$

$$T_\alpha = \frac{1}{10c} \int d^3r \, [(\mathbf{r} \cdot \mathbf{J}) r_\alpha - 2r^2 J_\alpha]. \tag{8}$$

Here, ω is the angular frequency, c is the speed of light and $\mathbf{r}$ specifies the location where the induced current $\mathbf{J}$ is evaluated and $\alpha, \beta = x, y, z$. The radiation power of each pole can be calculated as: $\sigma_P = \frac{\mu_0 \omega^4}{12\pi c} |\mathbf{P}|^2$, $\sigma_M = \frac{\mu_0 \omega^4}{12\pi c} |\mathbf{M}|^2$, and $\sigma_T = \frac{\mu_0 \omega^4 k^2}{12\pi c} |\mathbf{T}|$, with μ_0 being the permeability of vacuumnd k the wavevector.

Appendix 4: Effective mode volume for TD and MD BICs

In order to interpret the variation in the sensitivity of our metasurfaces, we give in Fig. 8 the effective mode volume of TD and MD modes as a function of structural parameters corresponding with those of Fig. 7. This confirms the intrinsic link between the mode volume and the sensitivity.

Optics EXPRESS

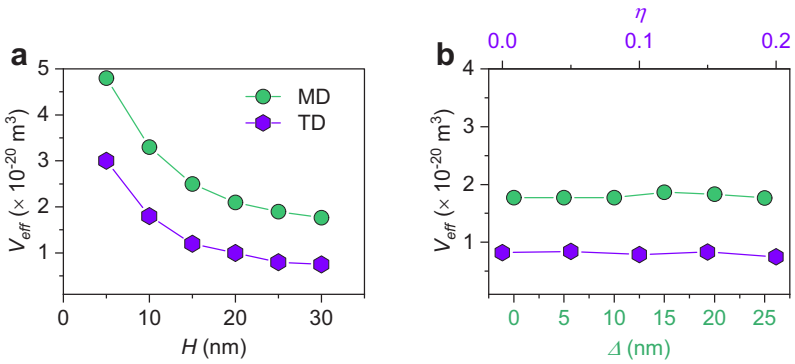

Fig. 8. (a) The effective eigenmode volume for TD and MD BICs versus the WS_2 thickness H. (b) The TD-BIC mode volume versus the parameter η associated with the gap width, and the MD-BIC mode volume versus the offset Δ.

Appendix 5: Sensing performance for freestanding WS_2 metasurfaces

Figure 9 presents detailed calculations with respect to the refractive index sensitivity for freestanding TD-BIC metasurfaces with different WS_2 thickness. The structural parameters for the metasurface in Fig. 9(a) are same to those in Fig. 7(a). Particularly, given that the WS_2 material possesses a very low absorption loss in the atomic monolayer limit, thus leading to a small absorption amplitude, and the TD quasi-BIC resonance shows an evident blueshift as the

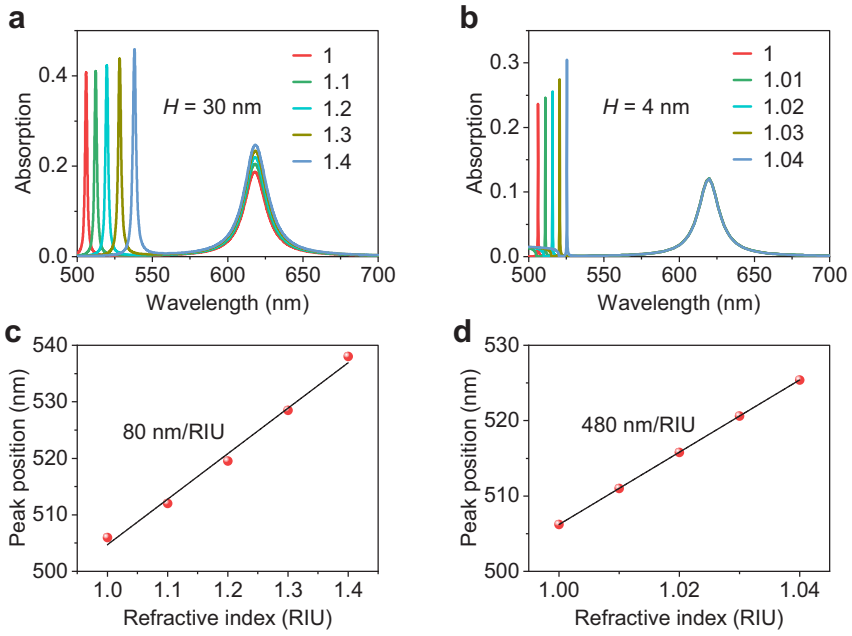

Fig. 9. (a, b) Absorption spectra of the freestanding TD-BIC metasurfaces with a WS_2 thickness of (a) $H = 30$ nm and (b) $H = 4$ nm. The different curves correspond to different values of the refractive index of the surroundings. (c, d) Resonance wavelength as a function of refractive index for the TD quasi-BIC mode in the metasurfaces with (c) $H = 30$ nm and (d) $H = 4$ nm. The black lines are liner fit to the dots.

Optics EXPRESS

WS_2 thickness is substantially reduced, the period and thickness of the metasurface in Fig. 9(b) are set as $P = 500$ nm and $H = 4$ nm, respectively.

Funding. National Natural Science Foundation of China (62105095, U1804261); Natural Science Foundation of Henan Province (202300410238); National Scientific Research Project Cultivation Fund of Henan Normal University (20210381, 2021PL22); Program for Innovative Research Team (in Science and Technology) in University of Henan Province (23IRTSTHN013).

Disclosures. The authors declare no conflicts of interest.

Data availability. Data underlying the results presented in this paper are not publicly available at this time but may be obtained from the authors upon reasonable request.

References

1. C. W. Hsu, B. Zhen, A. D. Stone, J. D. Joannopoulos, and M. Soljačić, "Bound states in the continuum," Nat. Rev. Mater. **1**(9), 16048 (2016).
2. K. Koshelev, G. Favraud, A. Bogdanov, Y. Kivshar, and A. Fratalocchi, "Nonradiating photonics with resonant dielectric nanostructures," Nanophotonics **8**(5), 725–745 (2019).
3. A. Kodigala, T. Lepetit, Q. Gu, B. Bahari, Y. Fainman, and B. Kanté, "Lasing action from photonic bound states in continuum," Nature **541**(7636), 196–199 (2017).
4. S. Romano, M. Mangini, E. Penzo, S. Cabrini, A. C. De Luca, I. Rendina, V. Mocella, and G. Zito, "Ultrasensitive surface refractive index imaging based on quasi-bound States in the continuum," ACS Nano **14**(11), 15417–15427 (2020).
5. S. Romano, G. Zito, S. Torino, G. Calafiore, E. Penzo, G. Coppola, S. Cabrini, I. Rendina, and V. Mocella, "Label-free sensing of ultralow-weight molecules with all-dielectric metasurfaces supporting bound states in the continuum," Photonics Res. **6**(7), 726–733 (2018).
6. S.-G. Lee, S.-Y. Jung, H.-S. Kim, S. Lee, and J.-M. Park, "Electromagnetically induced transparency based on guided-mode resonances," Opt. Lett. **40**(18), 4241–4244 (2015).
7. K. Koshelev, Y. Tang, K. Li, D.-Y. Choi, G. Li, and Y. Kivshar, "Nonlinear metasurfaces governed by bound states in the continuum," ACS Photonics **6**(7), 1639–1644 (2019).
8. L. Xu, K. Z. Kamali, L. Huang, M. Rahmani, A. Smirnov, R. Camacho-Morales, Y. Ma, G. Zhang, M. Woolley, D. Neshev, and A. E. Miroshnichenko, "Dynamic nonlinear image tuning through magnetic dipole quasi-BIC ultrathin resonators," Adv. Sci. **6**(15), 1802119 (2019).
9. H. Tang, C. DeVault, S. A. Camayd-Muñoz, Y. Liu, D. Jia, F. Du, O. Mello, D. I. Vulis, Y. Li, and E. Mazur, "Low-loss zero-index materials," Nano Lett. **21**(2), 914–920 (2021).
10. C.-L. Zou, J.-M. Cui, F.-W. Sun, X. Xiong, X.-B. Zou, Z.-F. Han, and G.-C. Guo, "Guiding light through optical bound states in the continuum for ultrahigh-Q microresonators," Laser Photonics Rev. **9**(1), 114–119 (2015).
11. S. I. Azzam, V. M. Shalaev, A. Boltasseva, and A. V. Kildishev, "Formation of bound states in the continuum in hybrid plasmonic-photonic systems," Phys. Rev. Lett. **121**(25), 253901 (2018).
12. Z. Liu, Y. Xu, Y. Lin, J. Xiang, T. Feng, Q. Cao, J. Li, S. Lan, and J. Liu, "High-Q quasibound states in the continuum for nonlinear metasurfaces," Phys. Rev. Lett. **123**(25), 253901 (2019).
13. Y. He, G. Guo, T. Feng, Y. Xu, and A. E. Miroshnichenko, "Toroidal dipole bound states in the continuum," Phys. Rev. B **98**(16), 161112 (2018).
14. K. Koshelev, S. Lepeshov, M. Liu, A. Bogdanov, and Y. Kivshar, "Asymmetric metasurfaces with high-Q resonances governed by bound states in the continuum," Phys. Rev. Lett. **121**(19), 193903 (2018).
15. Z. Sadrieva, K. Frizyuk, M. Petrov, Y. Kivshar, and A. Bogdanov, "Multipolar origin of bound states in the continuum," Phys. Rev. B **100**(11), 115303 (2019).
16. M. Chhowalla, D. Jena, and H. Zhang, "Two-dimensional semiconductors for transistors," Nat. Rev. Mater. **1**(11), 16052 (2016).
17. F. Withers, O. Del Pozo-Zamudio, A. Mishchenko, A. P. Rooney, A. Gholinia, K. Watanabe, T. Taniguchi, S. J. Haigh, A. K. Geim, A. I. Tartakovskii, and K. S. Novoselov, "Light-emitting diodes by band-structure engineering in van der Waals heterostructures," Nat. Mater. **14**(3), 301–306 (2015).
18. G. Eda and S. A. Maier, "Two-dimensional crystals: managing light for optoelectronics," ACS Nano **7**(7), 5660–5665 (2013).
19. A. Krasnok, S. Lepeshov, and A. Alú, "Nanophotonics with 2D transition metal dichalcogenides [Invited]," Opt. Express **26**(12), 15972–15994 (2018).
20. D. Zheng, S. Zhang, Q. Deng, M. Kang, P. Nordlander, and H. Xu, "Manipulating coherent plasmon−exciton interaction in a single silver nanorod on monolayer WSe_2," Nano Lett. **17**(6), 3809–3814 (2017).
21. R. Gogna, L. Zhang, Z. Wang, and H. Deng, "Photonic crystals for controlling strong coupling in van der Waals materials," Opt. Express **27**(16), 22700–22707 (2019).
22. M. Nauman, J. Yan, D. de Ceglia, M. Rahmani, K. Z. Kamali, C. De Angelis, A. E. Miroshnichenko, Y. Lu, and D. N. Neshev, "Tunable unidirectional nonlinear emission from transition-metal-dichalcogenide metasurfaces," Nat. Commun. **12**(1), 5597 (2021).

Optics EXPRESS

23. X. Zhang, C. De-Eknamkul, J. Gu, A. L. Boehmke, V. M. Menon, J. Khurgin, and E. Cubukcu, "Guiding of visible photons at the ångström thickness limit," Nat. Nanotechnol. **14**(9), 844–850 (2019).
24. X. Zong, L. Li, and Y. Liu, "Bound states in the continuum in all-van der Waals photonic crystals: a route enabling electromagnetically induced transparency," Opt. Express **30**(11), 17897–17908 (2022).
25. T. D. Green, D. G. Baranov, B. Munkhbat, R. Verre, T. Shegai, and M. Käll, "Optical material anisotropy in high-index transition metal dichalcogenide Mie nanoresonators," Optica **7**(6), 680–686 (2020).
26. R. Verre, D. G. Baranov, B. Munkhbat, J. Cuadra, M. Käll, and T. Shegai, "Transition metal dichalcogenide nanodisks as high-index dielectric Mie nanoresonators," Nat. Nanotechnol. **14**(7), 679–683 (2019).
27. V. Liu and S. Fan, "S4: A free electromagnetic solver for layered periodic structures," Comput. Phys. Commun. **183**(10), 2233–2244 (2012).
28. B. Munkhbat, D. G. Baranov, M. Stührenberg, M. Wersäll, A. Bisht, and T. Shegai, "Self-hybridized exciton-polaritons in multilayers of transition metal dichalcogenides for efficient light absorption," ACS Photonics **6**(1), 139–147 (2019).
29. V. Savinov, V. A. Fedotov, and N. I. Zheludev, "Toroidal dipolar excitation and macroscopic electromagnetic properties of metamaterials," Phys. Rev. B **89**(20), 205112 (2014).